Mineralogical Magazine (2019), **83**, 419–426
doi:10.1180/mgm.2018.158

CAMBRIDGE UNIVERSITY PRESS

Article

Discovery of Se-rich canfieldite, $Ag_8Sn(S,Se)_6$, from the Shuangjianzishan Ag–Pb–Zn deposit, NE China: A multimethodic chemical and structural study

Degao Zhai[1], Luca Bindi[2]*, Panagiotis C. Voudouris[3], Jiajun Liu[1], Stylianos F. Tombros[4] and Kuan Li[1]

[1]School of Earth Sciences and Resources, China University of Geosciences, 100083, Beijing, China; [2]Dipartimento di Scienze della Terra, Università di Firenze, Via La Pira 4, I-50121, Firenze, Italy; [3]Department of Mineralogy-Petrology, National and Kapodistrian University of Athens, 15784, Athens, Greece; and [4]Department of Geology, University of Patras, Rion, 26500, Patras, Greece

Abstract

During a study of the ore minerals belonging to the recently discovered Shuangjianzishan Ag–Pb–Zn deposit in NE China, we have discovered exceptional selenium enrichment in canfieldite (up to 11.6 wt.% of Se). Incorporation of Se into canfieldite has been investigated by an integrated approach using field emission scanning electron microscopy, electron microprobe and single-crystal X-ray diffraction. Canfieldite has been identified as one of the dominant Ag-bearing ore minerals in the studied deposit, which occurs mostly in slate-hosted vein type Ag–Pb–Zn ore bodies. Selenium is either homogeneously or, remarkably, heterogeneously distributed in the different canfieldite fragments studied. Chemical variations of Se are mostly attributable to a series of retrograde reactions resulting in diverse decomposition and exsolution of primary phases during cooling, or alternatively, related to influxes of Se-rich fluids during the formation of canfieldite. To evaluate the effects of the Se-for-S substitution in the structure, a crystal of Se-rich canfieldite $[Ag_{7.98}Sn_{1.02}(S_{4.19}Se_{1.81})_{\Sigma 6.00}]$ was investigated. The unit-cell parameters are: $a = 10.8145(8)$ Å and $V = 1264.8(3)$ Å^3. The structure was refined in the space group $F\bar{4}3m$ to $R_1 = 0.0315$ for 194 independent reflections, with 20 parameters. The crystal structure of Se-rich canfieldite was found to be topologically identical to that of pure canfieldite. If the short Ag–Ag contacts are ignored (due to the disorder), the two Ag atoms in the structure can be considered as three-fold (Ag1) and four-fold (Ag2) coordinated. Tin adopts a regular tetrahedral coordination. As in the case of Te-rich canfieldite, the refinement of the site-occupancy factor indicates that Se is disordered over the three anion positions.

Keywords: Se-rich canfieldite, chemical composition, crystal structure, Shuangjianzishan, Ag–Pb–Zn deposit, NE China

(Received 7 August 2018; Revised 8 September 2018; Accepted Manuscript Online 8 October 2018; Associate Editor: František Laufek)

Introduction

Canfieldite, Ag_8SnS_6, is a rare silver-bearing sulfosalt mineral which typically contains variable amounts of germanium substitution at the tin site and tellurium at the sulfur site. This mineral has been identified as one of the dominant Ag-bearing minerals in the recently discovered large Shuangjianzishan Ag–Pb–Zn deposit in NE China (Kuang *et al.*, 2014; Wu *et al.*, 2014). Furthermore, canfieldite in this deposit exhibits an exceptional enrichment in selenium.

Canfieldite is one of the five members of the argyrodite group, the other four members are argyrodite (Ag_8GeS_6; Weisbach, 1886), alburnite ($Ag_8GeTe_2S_4$; Tămaş *et al.*, 2014), putzite $[(Cu_{4.7}Ag_{3.3})_{\Sigma 8}GeS_6$; Paar *et al.*, 2004] and spryite ($Ag_8As^{3+}_{0.5}As^{5+}_{0.5}S_6$; Bindi *et al.*, 2017). Argyrodite and canfieldite are found to contain appreciable amounts of Te substituting for S, while in alburnite, Te appears to be ordered at specific structural sites (Tămaş *et al.*, 2014). Tellurium-rich canfieldite has been reported from several localities, e.g. Revelstoke, Canada (Harris and Owens, 1971), Nakatatsu mine, Japan (Marioko, 1981), Roşia Montană deposit, Romania (Popescu and Neacşu, 2011), Cirotan mine, Indonesia (Milési *et al.*, 1994), Panasqueira deposit, Portugal (Dykqs, 1985) and Lengenbach quarry, Binntal, Switzerland (Bindi *et al.*, 2012). From the structural point of view, Bindi *et al.* (2012) showed that Te does not occupy specific positions in the canfieldite structure, but it exhibits a disorder among the three available anion positions of the cubic $F\bar{4}3m$ structure. Although a very similar structural response is expected for the Se-for-S substitution, it is of interest to verify such a behaviour, even though Se-bearing varieties of canfieldite have been reported rarely, and then only from occurrences in the ex USSR (e.g. Nekrasova and Borodaev, 1972).

The present study aims to primarily provide a crystal-chemical characterisation of Se-rich canfieldite, and to clarify the structural role of selenium in these minerals by a multimethodic approach using a field emission scanning electron microprobe (FESEM), electron microprobe analyses (EMPA) and single-crystal X-ray diffraction (SCXRD).

Regional and deposit geology

The Shuangjianzishan Ag–Pb–Zn deposit is located in the southern segment of the Great Hinggan Range Metallogenic Belt in NE

*Author for correspondence: Luca Bindi, Email: luca.bindi@unifi.it
Cite this article: Zhai D., Bindi L., Voudouris P.C., Liu J., Tombros S.F. and Li K. (2019) Discovery of Se-rich canfieldite, $Ag_8Sn(S,Se)_6$, from the Shuangjianzishan Ag–Pb–Zn deposit, NE China: A multimethodic chemical and structural study. *Mineralogical Magazine* **83**, 419–426. https://doi.org/10.1180/mgm.2018.158

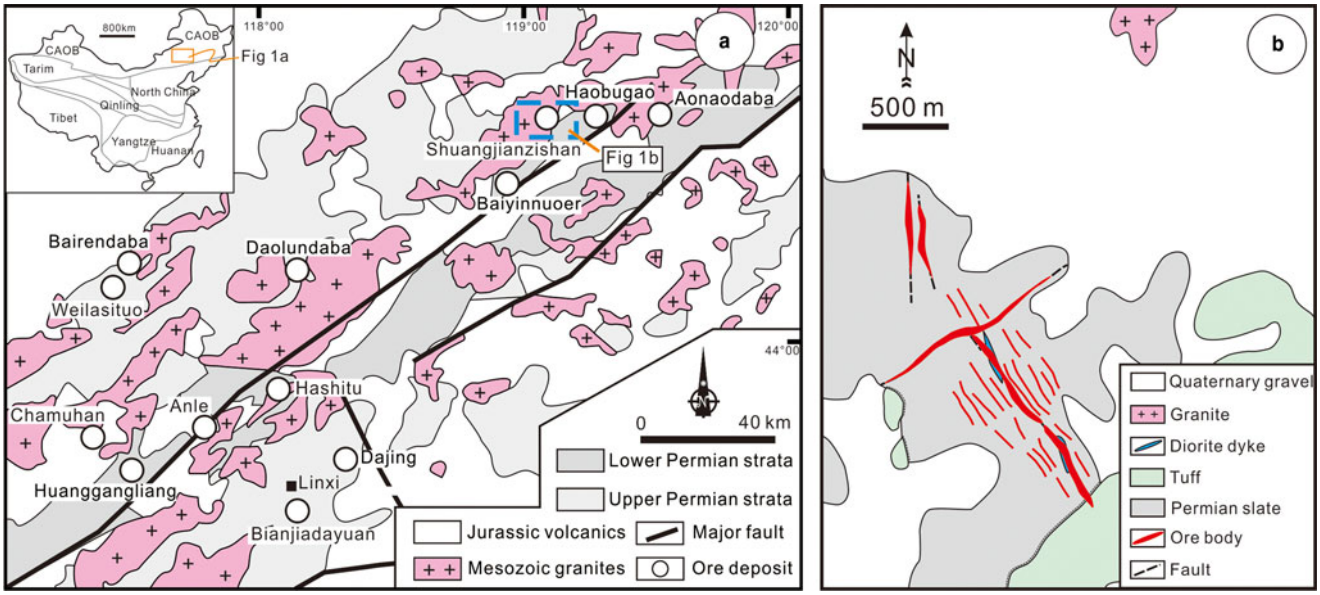

Fig. 1. (*a*) Geological map of the southern Great Hinggan Range in NE China showing the distributions of the Mesozoic granites and the locations of major ore deposits (modified from Zhai *et al.*, 2017); (*b*) Simplified geologic map of the Shuangjianzishan Ag–Pb–Zn deposit (based on Wu *et al.*, 2014). CAOB = Central Asian Orogenic Belt.

China, which lies in the easternmost segment of the Central Asian Orogenic Belt (Fig. 1*a*). The Central Asian Orogenic Belt evolved through complex closure of the Paleo-Asian Ocean from the Neoproterozoic to the late Phanerozoic (Wilde, 2015). This region records complex processes of tectonic events that marked the transition from the dominantly NE–SW directed motion of the Paleo-Asian plate to the E–W directed motion of the Paleo-Pacific plate (Wilde, 2015; Zhou *et al.*, 2017 and references therein). The tectonic evolution of the Central Asian Orogenic Belt since the late Permian can be summarised briefly as follows: (1) closure of the Paleo-Asian Ocean was completed in the Late Permian (~260 Ma); (2) a switch in geodynamic setting in the Late Permian to Early Triassic (~260–250 Ma) reflected by the Paleo-Asian Ocean closure and the onset of tectonics associated with subduction of the Paleo-Pacific plate; (3) events associated with the westward advance of the Paleo-Pacific plate dominated in the Early Jurassic to Early Cretaceous (~250–140 Ma); and (4) the Paleo-Pacific plate retreated eastwards after the Early Cretaceous (~140 Ma), resulting in an extensional setting associated with regional thinning and delamination of the lithosphere in NE China (e.g. Li, 2006; Wu *et al.*, 2011; Wilde, 2015; Zhou *et al.*, 2017; Liu *et al.*, 2017 and references therein).

The southern segment of the Great Hinggan Range Metallogenic Belt hosts a number of porphyry Mo–(Cu), skarn Fe–(Sn), and polymetallic (Ag–Pb–Zn–Cu) epithermal and hydrothermal vein deposits (Fig. 1*a*; Ouyang *et al.*, 2015; Shu *et al.*, 2016; Chen *et al.*, 2017; Gao *et al.*, 2017; Zhai *et al.*, 2014*a*,*b*, 2018*a*, 2019). These deposits are hosted mainly by Permian strata (e.g. slate, sandstone, siltstone, mudstone and carbonates) and Mesozoic granites (Fig. 1*a*) produced during regional Mesozoic magmatism (Mao *et al.*, 2014; Ouyang *et al.*, 2015; Zhai *et al.*, 2017; Gao *et al.*, 2017 and references therein). Recent exploration has revealed that Ag–Pb–Zn vein-type deposits are predominantly common in this region (Fig. 1*a*), which has led to new discoveries of the Shuangjianzishan, Bianjiadayuan, Bairendaba and Weilasituo deposits (e.g. Ouyang *et al.*, 2014; Liu *et al.*, 2016; Zhai *et al.*, 2017, 2018*b*), defining the southern segment of the Great Hinggan Range as the most important Ag–Pb–Zn polymetallic metallogenic belt in northern China. The ore deposits in this region are related mostly to Jurassic to Cretaceous magmatism (Mao *et al.*, 2014; Ouyang *et al.*, 2015; Gao *et al.*, 2017), and regionally, both mineralisation and Mesozoic (Jurassic to Cretaceous) granites demonstrate a close spatial distribution (Fig. 1*a*).

The main rocks exposed in the Shuangjianzishan ore district are composed of late Permian strata, the Mesozoic granites and volcanics, and the Quaternary paleo-placers (Fig. 1*b*). The strata in the ore district belong to the Dashizhai Formation, which consists mainly of argillaceous and sandy slate with a thickness of >950 m, which generally strike NE and dip NW with dipping angles of 55–65°. The Permian strata are the main ore-host rocks (Fig. 1*b*). The Mesozoic volcanics, of probable Jurassic age (Wu *et al.*, 2014), are located mainly in the southeast of the Ag–Pb–Zn mineralised zones. They demonstrate an unconformable contact relationship with the underlying Permian slates (Fig. 1*b*). These volcanic rocks consist largely of rhyolitic tuff and ignimbrite with a thickness of >200 m. A large volume of Quaternary gravels, which consist of unsorted rock fragments with a thickness of 15–50 m, are widespread in the ore district (Fig. 1*b*). Intrusive rocks are rare in the ore district, and the only exposed one is a granite intrusion located 2 km to the north of the ore deposit (Fig. 1*b*). Diorites mainly occur as dykes in the ore district, and strike NW or NE with a length of 50–300 m and a width of 1–8 m. Several diorite dykes are crosscut by the mineralised veins. The major faults in the ore district are NW-, NE- and NS-trending, and the Shuangjianzishan Ag–Pb–Zn veins are controlled primarily by NW-trending faults (Fig. 1*b*). Several ore bodies are also dominated by the NE-trending faults.

The Shuangjianzishan Ag–Pb–Zn deposit was first discovered in 2013. More than 70 major veins, and numerous stockworks and disseminations have been identified at the Shuangjianzishan ore district, all of which are hosted by the Permian slate. According to the recent 2018 exploration report, a total resource of 161.2 Mt ores have been discovered at Shuangjianzishan, and

the identified Ag reserve is >18.6 kt with an average grade of 128.5 g/t, the Pb reserve is 0.85 Mt (average grade of 0.6%) and the Zn reserve is 1.91 Mt (average grade of 1.6%), making this deposit the largest Ag deposit in China as well as in Asia (Kuang *et al.*, 2014). The identified Ag–Pb–Zn ores are hosted primarily by NW-trending open-space filling veins, which commonly strike 312° and dip NE with dipping angles of 50–60°. The ore bodies usually occur as parallel veins with a length between 100 and 800 m, and extend vertically at a depth greater than 500 m. Their widths vary usually from 1 to 10 m. Hydrothermal alteration is dominantly characterised by an assemblage of 'sericite', chlorite, quartz, calcite and illite (or smectite). Alteration halos are distributed asymmetrically on both sides of the mineralised veins. The spatial alteration zonation is commonly not apparent as alteration assemblages are superimposed upon one another.

Occurrence of canfieldite

Systematic microscopic observations identify that canfieldite, argentite and freibergite are the most abundant and widely distributed Ag-bearing ore minerals in the deposit studied (Fig. 2*a*, *b*), making up roughly >80 vol.% of the total Ag-bearing ores. Canfieldite is usually present independently (Fig. 2*a*) or associated with argentite and freibergite (Fig. 2*b*), which commonly replaces the earlier formed sulfides (sphalerite, galena and pyrite) along their mineral boundaries, or occur along cracks in those sulfides (Fig. 2*a*,*b*), showing that the Ag-bearing minerals mostly formed in a relatively late sequence compared to the base-metal sulfides. Canfieldite is also intergrown with other Ag-bearing minerals, occurring in lesser amounts in the mineralisation, e.g. polybasite, stephanite and pyrargyrite (Fig. 2*b*). In some cases, canfieldite can also be crosscut, rimmed, and replaced by galena (Fig. 3*a*,*b*), suggesting that insignificant canfieldite may also occur in the early ore stage associated with sulfides. Commonly, canfieldite occurs as small anhedral grains (20–50 μm). However, it can occasionally also occur as relatively coarse grains (>500 μm) associated with galena and sphalerite (Fig. 3*a*).

Based on field vein crosscutting relationships and the mineral assemblages, the Ag–Pb–Zn mineralisation at Shuangjianzishan can be divided into three distinct ore stages: (I) early pre-ore pyrite + quartz ± K-feldspar; (II) main ore sulfide + sulfosalt + quartz + calcite + 'sericite' + chlorite ± illite ± epidote; and (III) post-ore quartz + pyrophyllite + kaolinite (Fig. 4). In addition, stage II could be divided further into two sequences, substages II-1 and II-2 (Fig. 4). The early sequence (stage II-1) consists of ore minerals of galena + sphalerite + pyrite + chalcopyrite ± canfieldite ± freibergite, which are associated closely with alteration/gangue assemblages of quartz + calcite + chlorite ± epidote ± illite ± 'sericite'. The subsequent ore sequence (stage II-2) is composed dominantly of a series of silver-bearing ore minerals (mainly abundant sulfosalts and argentite) ± pyrrhotite ± galena ± sphalerite ± chalcopyrite. The silver-bearing minerals are associated spatially with alteration/gangue mineral assemblages composed of quartz + 'sericite' ± calcite ± chlorite. The late sequence in stage II is the most important period for extensive Ag precipitation in the deposit.

Analytical methods

Sixty polished thin sections were examined in reflected and transmitted light from the samples collected from different mining levels and drill holes from the Shuangjianzishan deposit. A

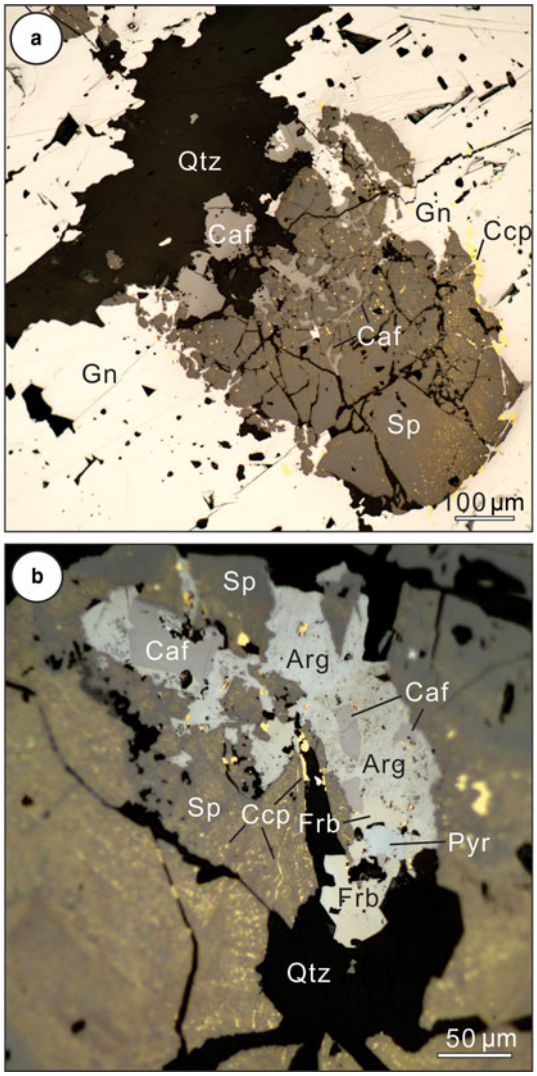

Fig. 2. Reflected light photomicrographs of sulfides and silver-bearing ore minerals from the Shuangjianzishan deposit. (*a*) Canfieldite crosscuts sphalerite and galena; (*b*) canfieldite with association of argentite, freibergite and pyrargyrite fill cracks in sphalerite. Abbreviations: Arg – argentite; Caf – canfieldite; Ccp – chalcopyrite; Frb – freibergite; Gn – galena; Pyr – pyrargyrite; Qtz – quartz; Sp – sphalerite.

FESEM, a Zeiss Supra 55 Sapphire, at the China University of Geosciences Beijing (CUGB) was used to image ore textures and determine mineral compositions semi-quantitatively for the purpose of identification. Element line scanning using energy dispersive spectroscopy (EDS) was undertaken for Ag*Lα*, Sb*Lα*, Pb*Mα*, Fe*Kα*, Sn*Lα*, Se*Lα* and S*Kα*. The accelerating voltage was 20 kV and the working distance 15 mm. Compositions of canfieldite were determined using a JEOL 8230 Superprobe equipped with EDS, wavelength dispersive spectroscopy (WDS), and a back-scatter electron detector at the Chinese Academy of Geological Sciences (CAGS). The accelerating voltage was 20 kV. Beam current and count times for major elements were 20 nA and 20 s, respectively (10 s for background measurement), and beam size was 1 μm. The detection limits were 155 ppm for Au, 210 ppm for Ag, 400 ppm for Cu, 150 ppm for Fe, 300 ppm for Co, 130 ppm for Ni, 90 ppm for Se and 260 ppm for Te. Natural and synthetic mineral standards (chalcopyrite, sphalerite, galena, pyrrhotite, InAs and native Ag, Sb, Se and Sn) were utilised for calibration. X-ray lines measured were

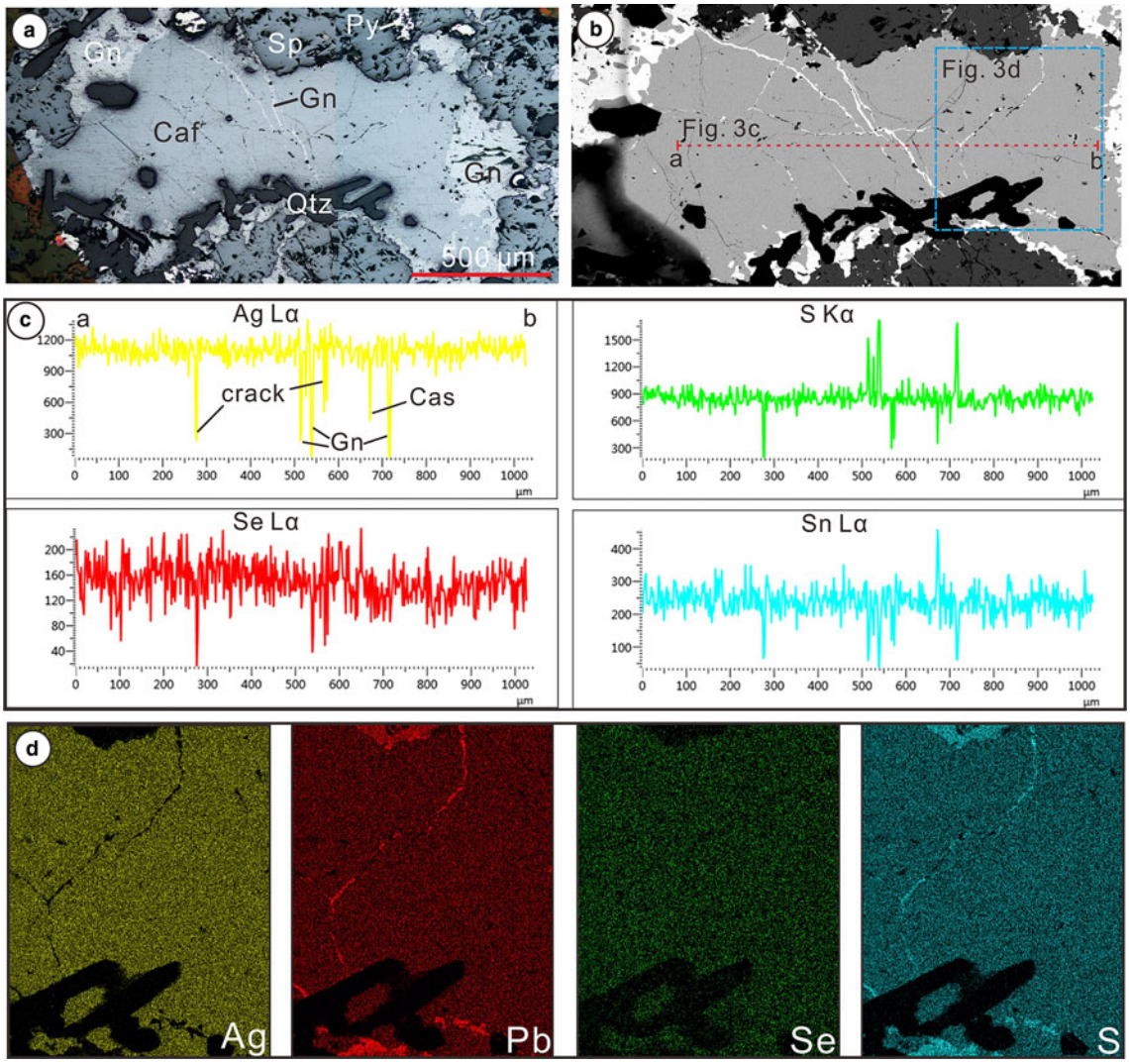

Fig. 3. Occurrence of Se-rich canfieldite from the Shuangjianzishan Ag–Pb–Zn deposit. (*a*) A large canfieldite grain intergrown with galena, sphalerite and quartz (reflected light); (*b*) The same mineral to (*a*) in BSE, and the locations for element line scanning and mapping for (*c*) and (*d*) are shown; (*c*) element line scanning patterns of Ag, S, Se and Sn, and the different patterns revealing cracks and mineral inclusions of galena and cassiterite in canfieldite; (*d*) element mapping patterns of Ag, Pb, Se and S for canfieldite. Abbreviations: Caf – canfieldite; Cas – cassiterite; Gn – galena; Py – pyrite; Qtz – quartz; and Sp – sphalerite.

Ag*L*α, Sb*L*α, As*L*α, Pb*L*α, Zn*L*α, Sn*L*α, Fe*K*α, Cu*K*α, Se*K*α and S*K*α. The analytical results for numerous Se-bearing canfieldite grains, along with sample numbers, are listed in Supplementary Table S1 (see below). X-ray element mapping was performed using an energy-dispersive X-ray detector on the JEOL 8230 Superprobe at CAGS. The dwell time was set to 20 μs to provide the highest possible resolution.

The crystal richest in Se (Fig. 3*a*) was handpicked from the rock sample and preliminarily rechecked with the electron microprobe. Major and minor elements were determined using a JEOL-JXA electron microprobe. The analytical conditions were 20 kV accelerating voltage and 40 nA beam current, with 30 s counting time. For the WDS analyses the following lines were used: Ag*L*α, Sn*L*α, Se*K*α and S*K*α. The estimated analytical precision is: ± 0.40 for Ag, ± 0.30 for Sn and ± 0.20 for Se and S. Pure elements were used for all standards. The canfieldite fragment was found to be homogeneous within analytical error. The average chemical composition for the crystal with the largest amount of Se (5 analyses on different spots), together with ranges of wt.% of elements, is reported in Table 1. On the basis of 15 atoms, the formula can be written as $Ag_{7.98}Sn_{1.02}(S_{4.19}Se_{1.81})_{\Sigma 6.00}$. The same crystal was then examined by means of an Oxford Xcalibur single-crystal diffractometer using graphite-monochromatised Mo*K*α radiation. Intensity integration, standard Lorentz polarisation and absorption correction were performed with the *Crysalis* (Oxford Diffraction, 2006) software package. Given the similarities in the unit-cell, cubic symmetry and reflections conditions between the examined crystal and Te-rich canfieldite (Bindi *et al.*, 2012), the crystal-structure refinement was carried out starting with the atom coordinates reported for the $F\bar{4}3m$ structure of Te-rich canfieldite. The full-matrix least-squares program *SHELXL-97* (Sheldrick, 2008) was used for the refinement of the structure. The site occupancy of all the positions was allowed to vary using different couples of neutral Sn, Ag, S and Se scattering curves (Ibers and Hamilton, 1974). Similarly to Te-rich canfieldite (Bindi *et al.*, 2012), the Ag1 and Ag2 positions were found to be partially occupied, but an equation was added on the global Ag occupancy to fulfil the overall charge balance (i.e. Ag = 8.00 atoms per formula unit for $Z = 4$). At the last stage, with anisotropic

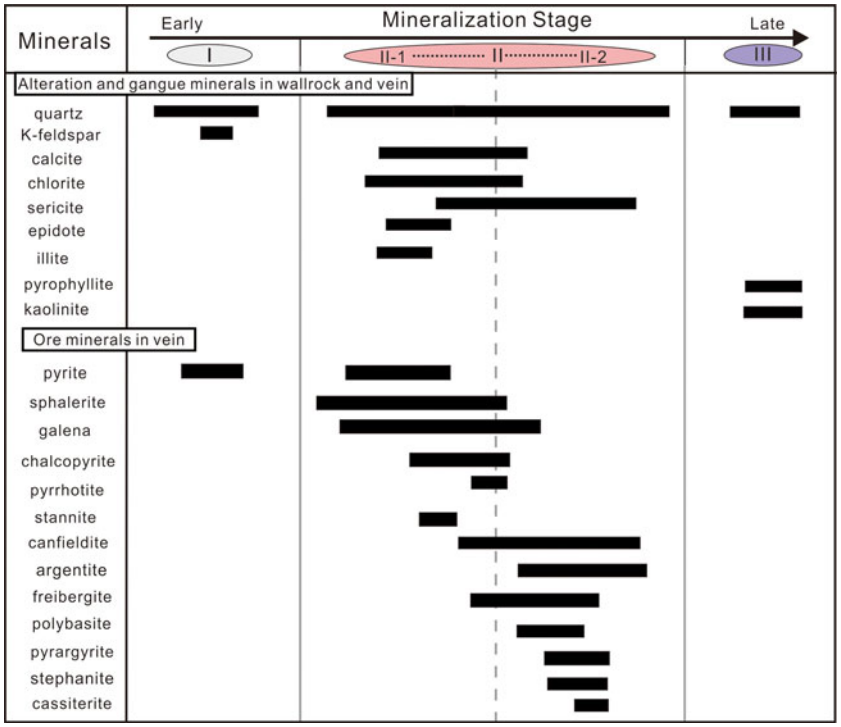

Fig. 4. Summary of the paragenetic sequence for the Shuangjianzishan Ag–Pb–Zn mineralisation.

atomic displacement parameters for all atoms and no constraints, the residual value settled at $R_1 = 0.0315$ for 189 observed reflections [$F_o > 4\sigma(F_o)$] and 20 refined parameters, and at $R_1 = 0.0327$ for all 194 independent reflections. The inspection of the difference-Fourier map revealed that maximum positive and negative peaks were 1.36 and 0.89 $e^-/Å^3$, respectively. Experimental details of the data collection and refinement are given in Table 2. Fractional atom coordinates and anisotropic-displacement parameters are shown in Table 3. Bond distances are reported in Table 4. The crystallographic information files have been deposited with the Principal Editor of *Mineralogical Magazine* and are available as Supplementary material (see below).

Results and discussion

Canfieldite chemistry, texture and origin

Measured compositions for canfieldite (Tables 1 and S1) demonstrate that Ag, Sn and S contents range commonly from 59.2 to 69.6, 9.05 to 19.3, and 10.4 to 21.5 wt.%, respectively. Analyses also show minor amounts of Cu, Fe, Zn, Ge, Au and Te in canfieldite (Tables 1 and S1). The Se contents show a relatively large variation from below the detection limit (0.01 wt.%) to

Table 1. Electron microprobe data for Se-rich canfieldite (means and ranges in wt.% of elements) and atoms per formula unit (apfu, on the basis of 15 atoms) with their standard deviations (σ) in parentheses.

	Mean	Range	Apfu (σ)
Ag	67.89	67.09–68.19	7.98 (0.22)
Sn	9.54	9.05–9.88	1.02 (0.11)
Ge	0.02	0.00–0.05	0.00 (0.00)
Zn	0.02	0.00–0.06	0.00 (0.00)
S	10.58	10.41–10.69	4.19 (0.09)
Se	11.26	11.15–11.56	1.81 (0.12)
Total	99.31	99.13–100.08	15.00

Table 2. Crystallographic data and refinement parameters for Se-rich canfieldite.

Crystal data	
Ideal formula	$Ag_8Sn(S,Se)_6$
Crystal system, space group	Cubic, $F\bar{4}3m$ (#216)
Unit-cell parameter, a (Å)	10.8145(8)
Unit-cell volume (Å^3)	1264.8(3)
Z	4
Temperature (K)	298(3)
Calculated density (g cm^{-3})	1.365
μ (mm^{-1})	21.17
Data collection	
Crystal size (mm)	0.080 × 0.070 × 0.055
Diffractometer	Oxford Xcalibur
Radiation, wavelength (Å)	Mo$K\alpha$, λ = 0.71073
2θ max for data collection (°)	56.58
Absorption correction method	ABSPACK (Oxford Diffraction, 2006)
T_{min}, T_{max}	0.925, 0.988
Crystal-to-detector distance (mm)	50
Axis, frames, width (°), time per frame (s)	ω–φ, 1264, 1.00, 30
No. of measured, independent and observed $F > 4\sigma(F)$ reflections	12,968, 194, 189
R_{int}	0.088
Data completeness to θ_{max} (%)	99.1
h, k, l ranges	$-14 \le h \le 14$, $-14 \le k \le 14$, $-14 \le l \le 14$
Refinement	
Refinement method	Full-matrix least-squares on F^2
Weighting scheme	$1/\sigma^2(F)$
Number of reflections, parameters, restraints	189/20/0
R_1 [$F > 4\sigma(F)$], R_1 (all)	0.0315, 0.0327
wR_2 [$F > 4\sigma(F)$], wR_2 (all)	0.0618, 0.0665
GoF on F^2	1.044
$\Delta\rho_{max}$, $\Delta\rho_{min}$ (e^- Å^{-3})	1.36, –0.88

$R_{int} = (n/n-1)^{1/2}\left[F_o^2 - F_o(mean)^2\right]/\sum F_o^2$

$R_1 = \sum ||F_o| - |F_c||/\sum |F_o| \qquad wR_2 = \left\{\sum\left[w(F_o^2 - F_c^2)^2\right]/\sum\left[w(F_o^2)^2\right]\right\}^{1/2}$

$GoF = \left\{\sum\left[w(F_o^2 - F_c^2)^2\right]/(n-p)\right\}^{1/2}$ where n = no. of reflections, p = no. of refined parameters

Table 3. Atoms, Wyckoff letter, site occupancy, fractional atom coordinates (Å) and atomic displacement parameters (Å^2) for Se-rich canfieldite.

Atom	Wyckoff	Site occupancy	*x*	*y*	*z*	U_{iso}	U^{11}	U^{22}	U^{33}	U^{23}	U^{13}	U^{12}
Sn	4*c*	$Sn_{1.00}$	¼	¼	¼	0.0243(7)	0.0243(7)	0.0243(7)	0.0243(7)	0	0	0
Ag1	24*f*	$Ag_{0.409}$	0.2216(3)	0	0	0.0297(9)	0.030(2)	0.030(1)	0.030(1)	−0.003(2)	0	0
Ag2	48*h*	$Ag_{0.462}$	0.4295(2)	0.4295(2)	0.7614(3)	0.0300(6)	0.0300(7)	0.0300(7)	0.030(1)	0.001(1)	0.0018(8)	−0.001(1)
*X*1	16*e*	$S_{0.73(5)}Se_{0.27}$	0.3749(4)	0.3749(4)	0.3749(4)	0.057(3)	0.057(3)	0.057(3)	0.057(3)	0.003(2)	0.003(2)	0.003(2)
*X*2	4*a*	$S_{0.60(7)}Se_{0.40}$	0	0	0	0.070(5)	0.070(5)	0.070(5)	0.070(5)	0	0	0
*X*3	4*d*	$S_{0.63(6)}Se_{0.37}$	¾	¾	¾	0.055(4)	0.055(4)	0.055(4)	0.055(4)	0	0	0

Table 4. Selected bond distances (Å) for Se-rich canfieldite.

Sn–*X*3	×4	2.339(8)	Ag1–*X*2		2.396(4)	Ag2–*X1*	×2	2.645(3)
			Ag1–*X*1	×2	2.532(3)	Ag2–*X*3		2.748(2)
			<Ag1–*X*>		2.487	Ag2–*X*2		2.797(3)
						<Ag2–*X*>		2.709

11.6 wt.%. In detail, the highest Se analyses are entirely from one large canfieldite grain (Fig. 3*a*), which shows homogeneous features (Fig. 3*b*) and, for this reason, was selected for the SCXRD study. The element line scanning of this large canfieldite grain reveals that Se, as well as other major elements (e.g. Ag and Sn), are distributed homogeneously (Fig. 3*c*), which is consistent with the results of the element mapping of part of this large canfieldite grain (Fig. 3*d*). Furthermore, cassiterite has also been identified as small mineral inclusions in canfieldite on the basis of element line scanning (Fig. 3*c*).

Numerous EMPA on distinct Se-bearing canfieldite grains, however, yield that Se is remarkably heterogeneous in canfieldite. This compositional inhomogeneity is evident on the trace-element maps of an individual grain (Fig. 5*a*–*d*), which show that both high- and low-Se domains exist (Fig. 5*b*). Similar patterns of heterogeneous Ag distribution in freibergite have been reported by

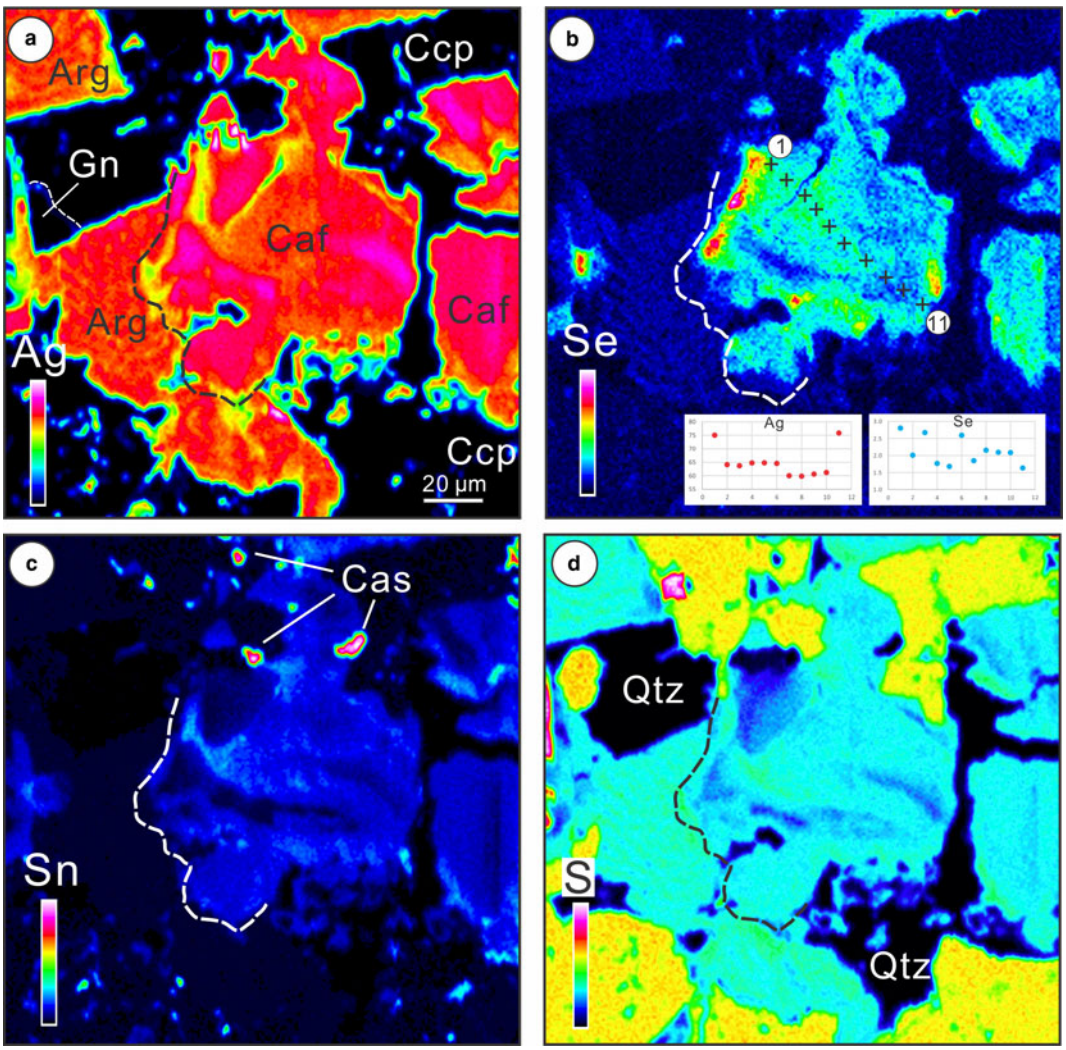

Fig. 5. Element mapping of Ag (*a*), Se (*b*), Sn (*c*) and S (*d*) for canfieldite. The positions and results for 11 EMPA along the mineral grain are shown in (*b*). Abbreviations: Arg – argentite; Caf – canfieldite; Cas – cassiterite; Ccp – chalcopyrite; Gn – galena; and Qtz – quartz.

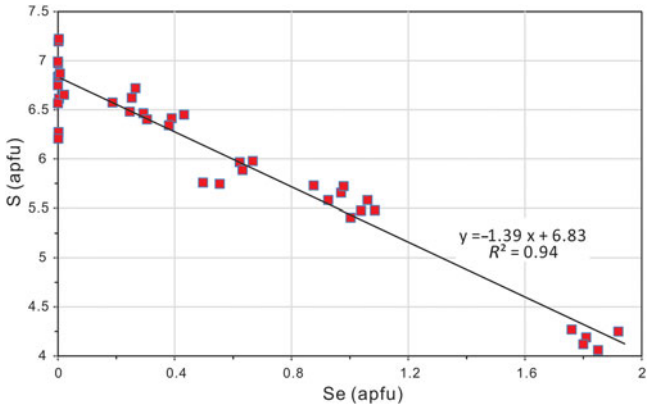

Fig. 6. Plot of Se *vs.* S contents in canfieldite (in atoms per formula unit).

Zhai *et al.* (2019) from a nearby Ag–Pb–Zn vein-type deposit in the southern Great Hinggan Range, which are mostly attributable to a series of retrograde reactions resulting in diverse decomposition and exsolution of primary phases during cooling. Similarly to freibergite, the observed chemical heterogeneity in canfieldite is probably related to the fact that we had originally a single grain that experienced exsolution and decomposition during its cooling. Alternatively, the compositionally zoned pattern could be related to influxes of Se-rich fluids during the formation of canfieldite. Finally, a very good negative correlation ($R^2 = 0.94$) between Se and S can be observed for canfieldite, suggesting an ideal Se-for-S substitution (Fig. 6), as also demonstrated from the structural study.

A number of EMPA of other Ag-bearing ore minerals (argentite, freibergite, polybasite, stephanite and pyrargyrite) produces Se contents normally below the detection limit, demonstrating that Se is almost entirely restricted to canfieldite in the deposit studied (Fig. 5*b*). However, the origin of Se in canfieldite precipitated from hydrothermal fluids is still unclear. The evident enrichment of Se in ore fluids at Shuangjianzishan most probably reflects a close genetic association with a magmatic body. For example, the presence of Se-bearing ore minerals in the Perama Hill high-sulfidation deposit in Greece has been suggested to be compatible with direct deposition of metals from the vapour phase of a degassing magmatic (porphyry) body (Voudouris *et al.*, 2011). Considering a regional ore district scale, the porphyry-epithermal ore system in NE Greece is characterised by a close spatial association among granitic intrusion centres, base-metal enrichment, and a trace-element signature that involves Ag, Au, Sn, Se, Te, Bi and Mo (Voudouris *et al.*, 2011). Furthermore, numerous magmatic-hydrothermal ore deposits adjacent to the studied deposit in the southern Great Hinggan Range, such as the Bianjiadayuan Ag–Pb–Zn, the Weilasituo Cu–Zn, the Huangangliang Fe, the Dajing Cu–Sn, and the Baiyinnuoer Pb–Zn deposits (Fig. 1*a*), all reflect proximity to, and a close genetic association with, a granitic porphyry/intrusion (Ouyang *et al.*, 2015; Zeng *et al.*, 2016; Zhai *et al.*, 2017). In addition, sulfur and lead isotope results suggest the origin of both sulfur and metals (Ag, Pb and Zn) in the Shuangjianzishan deposit from a granitic magmatism (Jiang *et al.*, 2017). Therefore, we suggest that Se enrichment in the Ag-bearing ore minerals is due to its derivation from a felsic magma, and could be regarded as a mineralogical indicator of a direct magmatic contribution.

Crystal-chemical remarks

The crystal structure of Se-rich canfieldite shows close similarities with that of Te-rich canfieldite (Bindi *et al.*, 2012). It is also topologically identical to that of putzite (Paar *et al.*, 2004) and that of the synthetic Cu_8GeS_6 cubic compound (Ishii *et al.*, 1999). It can be generally described as based on regular polyhedra such as $Sn(X)_4$, $(X)Ag_6$, $(X)Ag_{12}$ and $(X)Ag_{12}$, with $X = (S, Se)$. If we use the classic polyhedral description and ignore the short Ag–Ag contacts (due to the disorder of the two partially occupied silver positions), the Ag1 atom may be considered as three-fold coordinated with a mean Ag–*X* distance of 2.49 Å, a value very similar to that found for the Ag1 position in the crystal structure of Te-rich canfieldite (2.53 Å; Bindi *et al.*, 2012). The Ag2 atom adopts a close-to-tetrahedral coordination with an overall mean Ag–*X* distance of 2.71 Å, which is slightly smaller than that found for Te-rich canfieldite (2.76 Å; Bindi *et al.*, 2012), but perfectly matching the range of bond distances observed for the pearceite–polybasite group of minerals (range: 2.68–2.72 Å: Bindi *et al.*, 2006, 2007; Evain *et al.*, 2006).

The refinement of the site-occupancy factors indicated Se to be disordered among the three anion positions (Table 3), resulting in the formula $Ag_8Sn(S_{4.15}Se_{1.85})_{\Sigma 6}$, which is in excellent agreement with that obtained from microprobe data, $Ag_{7.98}Sn_{1.02}(S_{4.19}Se_{1.81})_{\Sigma 6.00}$. Bindi *et al.* (2012) observed that Te exhibited a site preference for *X*1; however we, on the contrary, observed no site preference for Se, indicating that the Bindi *et al.* (2012) Te-for-S substitution at *X*1 was not driven by any intrinsic difference in the anion environment. The Sn position shows a regular tetrahedral coordination, with a mean bond distance of 2.34 Å.

Acknowledgements. This research was supported financially by the National Natural Science Foundation of China (Grant 41672068), and by "Progetto di Ateneo 2015" of the University of Florence, Italy. Single-crystal diffraction studies were undertaken at CRIST, Centro di Cristallografia Strutturale, University of Florence, Italy. We thank Dongjie Tang (CUGB) for the SEM analyses, and Zhenyu Chen and Xiaodan Chen (CAGS) for the microprobe analyses. Meng Dai and Wenbin Jia are thanked for the field help and sample collections, and Nigel Cook and Wenyuan Liu for the discussions. Peter Leverett, Federica Zaccarini, and one anonymous reviewer are thanked for their helpful comments that improved this work. Editor Stuart Mills and Associate Editor František Laufek are thanked for their helpful suggestions.

Supplementary material. To view supplementary material for this article, please visit https://doi.org/10.1180/mgm.2018.158.

References

Bindi L., Evain M. and Menchetti S. (2006) Temperature dependence of the silver distribution in the crystal structure of natural pearceite, $(Ag,Cu)_{16}(As,Sb)_2S_{11}$. *Acta Crystallographica*, **B62**, 212–219.

Bindi L., Evain M. and Menchetti S. (2007) Complex twinning, polytypism and disorder phenomena in the crystal structures of antimonpearceite and arsenpolybasite. *The Canadian Mineralogist*, **45**, 321–333.

Bindi L., Nestola F., Guastoni A., Zorzi F., Peruzzo L. and Raber T. (2012) Te-rich canfieldite, $Ag_8Sn(S,Te)_6$, from Lengenbach quarry, Binntal, Canton Valais, Switzerland: Occurrence, description and crystal structure. *The Canadian Mineralogist*, **50**, 111–118.

Bindi L., Keutsch F.N., Morana M. and Zaccarini F. (2017) Spryite, $Ag_8(As^{3+}_{0.5}As^{5+}_{0.5})S_6$: structure determination and inferred absence of superionic conduction of the first As^{3+}-bearing argyrodite. *Physics and Chemistry of Minerals*, **44**, 75–82.

Chen Y.J., Zhang C., Wang P., Pirajno F. and Li N. (2017) The Mo deposits of Northeast China: a powerful indicator of tectonic settings and associated evolutionary trends. *Ore Geology Reviews*, **81**, 602–640.

Dykqs D. (1985) Silver minerals of Panasqueira, Portugal: a new occurrence of Te-bearing canfieldite. *Mineralogical Magazine*, **49**, 745–748.

Evain M., Bindi L. and Menchetti S. (2006) Structural complexity in minerals: twinning, polytypism and disorder in the crystal structure of polybasite, $(Ag,Cu)_{16}(Sb,As)_2S_{11}$. *Acta Crystallographica*, **B62**, 447–456.

Gao J., Klemd R., Zhu M., Wang X., Li J., Wan B., Xiao W., Zeng Q., Shen P., Sun J. and Qin K. (2017) Large-scale porphyry-type mineralization in the Central Asian metallogenic domain: A review. *Journal of Asian Earth Sciences*, **165**, 7–36.

Harris D.C. and Owens D.R. (1971) A tellurium-bearing canfieldite, from Revelstoke, BC. *The Canadian Mineralogist*, **10**, 895–898.

Ibers J.A. and Hamilton W.C. (editors) (1974) *International Tables for X-ray Crystallography*, vol. IV, 366 pp. Kynock, Dordrecht, The Netherlands.

Ishii M., Onoda M. and Shibata K. (1999) Structure and vibrational spectra of argyrodite family compounds Cu_8SiX_6 (X = S, Se) and Cu_8GeS_6. *Solid State Ionics*, **121**, 11–18.

Jiang B.B., Zhu X.Y., Huang X.K., Xu Q. and Zhang Z.Q. (2017) Isotopic characteristics of sulfur and lead and metallogenic mechanism of Shuangjianzishan silver polymetallic deposit in Inner Mongolia. *Mineral Exploration*, **8**, 1010–1019 [in Chinese with English abstract].

Kuang Y.S., Zheng G.R., Lu M.J., Liu Y.L., Zhang S.J., Li R.Y. and Cheng W.J. (2014) Basic characteristics of Shuangjianzishan silver polymetallic deposit in Chifeng City, Inner Mongolia. *Mineral Deposits*, **33**, 847–856 [in Chinese with English abstract].

Li J.Y. (2006) Permian geodynamic setting of Northeast China and adjacent regions: closure of the Paleo-Asian Ocean and subduction of the Paleo-Pacific Plate. *Journal of Asian Earth Sciences*, **26**, 207–224.

Liu C., Bagas L. and Wang F. (2016) Isotopic analysis of the super-large Shuangjianzishan Pb–Zn–Ag deposit in Inner Mongolia, China: Constraints on magmatism, metallogenesis, and tectonic setting. *Ore Geology Reviews*, **75**, 252–267.

Liu K., Zhang J., Wilde S. A., Zhou J., Wang M., Ge M., Wang J. and Ling Y. (2017) Initial subduction of the Paleo-Pacific Oceanic plate in NE China: Constraints from whole-rock geochemistry and zircon U-Pb and Lu-Hf isotopes of the Khanka Lake granitoids. *Lithos*, **274–275**, 254–270.

Mao J., Pirajno F., Lehmann B., Luo M. and Berzina A. (2014) Distribution of porphyry deposits in the Eurasian continent and their corresponding tectonic settings. *Journal of Asian Earth Sciences*, **79**, 576–584.

Marioko T. (1981) Silver distribution and silver-bearing minerals in the Nakayama and Hitokata ore deposits of the Nakatatsu mine, Fukui Prefecture, Japan. *Mining Geology, Special Issue*, **10**, 159–179.

Milési J.P., Marcoux E., Nehlig P., Sunarya Y., Sukandar A. and Felenc J. (1994) Cirotan, West Java, Indonesia; a 1.7 Ma hybrid epithermal Au-Ag-Sn-W deposit. *Economic Geology*, **89**, 227–245.

Nekrasova A.H. and Borodaev S. (1972) Pervaia nakhodka selensoderzhashchego kanfildita, *Doklady Akademy Nauk SSSR*, **203**, 907–910 [in Russian].

Ouyang H., Mao J., Santosh M., Wu Y., Hou L. and Wang X. (2014) The Early Cretaceous Weilasituo Zn–Cu–Ag vein deposit in the southern Great Xing'an Range, northeast China: Fluid inclusions, H, O, S, Pb isotope geochemistry and genetic implications. *Ore Geology Reviews*, **56**, 503–515.

Ouyang H., Mao J., Zhou Z. and Su H. (2015) Late Mesozoic metallogeny and intracontinental magmatism, southern Great Xing'an Range, northeastern China. *Gondwana Research*, **27**, 1153–1172.

Oxford Diffraction (2006) *CrysAlis RED (Version 1.171.31.2) and ABSPACK in CrysAlis RED*. Oxford Diffraction, Abingdon, Oxfordshire, England.

Paar W.H., Roberts A.C., Berlepsch P., Armbruster T., Topa D. and Zagler G. (2004) Putzite, $(Cu_{4.7}Ag_{3.3})_8GeS_6$, a new mineral species from Capillitas, Catamarca, Argentina: description and crystal structure. *The Canadian Mineralogist*, **42**, 1757–1769.

Popescu G.C. and Neacşu A. (2011) Preliminary data on two tin-sulfosalts (canfieldite and pirquitasite) from Roşia Montană. *Romanian Journal of Earth Sciences*, **85**, 35–41.

Sheldrick G.M. (2008) A short history of SHELX. *Acta Crystallographica*, **A64**, 112–122.

Shu Q., Chang Z., Lai Y., Zhou Y., Sun Y. and Yan C. (2016) Regional metallogeny of Mo-bearing deposits in northeastern China, with new Re-Os dates of porphyry Mo deposits in the northern Xilamulun district. *Economic Geology*, **111**, 1783–1798.

Tămaş C.G., Grobety B., Bailly L., Bernhardt H.J. and Minuţ A. (2014) Alburnite, $Ag_8GeTe_2S_4$, a new mineral species from the Roşia Montana Au-Ag epithermal deposit, Apuseni Mountains, Romania. *American Mineralogist*, **99**, 57–64.

Voudouris P.C., Melfos V., Spry P.G., Moritz R., Papavassiliou C. and Falalakis G. (2011) Mineralogy and geochemical environment of formation of the Perama Hill high-sulfidation epithermal Au-Ag-Te-Se deposit, Petrota Graben, NE Greece. *Mineralogy and Petrology*, **103**, 79–100.

Weisbach A. (1886) Argyrodit, ein neues Silbererz. *Neues Jahrbuch für Mineralogie, Geologie und Paläontologie*, **2**, 67–71.

Wilde S.A. (2015) Final amalgamation of the Central Asian Orogenic Belt in NE China: Paleo-Asian Ocean closure versus Paleo-Pacific plate subduction — A review of the evidence. *Tectonophysics*, **662**, 345–362.

Wu F.Y., Sun D.Y., Ge W.C., Zhang Y.B., Grant M.L., Wilde S.A. and Jahn B.M. (2011) Geochronology of the Phanerozoic granitoids in northeastern China. *Journal of Asian Earth Sciences*, **41**, 1–30.

Wu G., Liu J., Zeng Q., Liu M., Sun H., Yin Z. and Yin X. (2014) Occurrences of silver in the Shuangjianzishan Pb-Zn-Ag deposit and its implications for mineral processing. *Earth Science Frontiers*, **21**, 105–115 [in Chinese with English abstract].

Zeng Q., Liu J., Chu S., Guo Y., Gao S., Guo L. and Zhai Y. (2016) Poly-metal mineralization and exploration potential in southern segment of the Da Hinggan Mountains. *Journal of Jilin University (Earth Science Edition)*, **46**, 1100–1123 [in Chinese with English abstract].

Zhai D., Liu J., Wang J., Yang Y., Zhang H., Wang X., Zhang Q., Wang G. and Liu Z. (2014*a*) Zircon U-Pb and molybdenite Re-Os geochronology, and whole-rock geochemistry of the Hashitu molybdenum deposit and host granitoids, Inner Mongolia, NE China. *Journal of Asian Earth Sciences*, **79**, 144–160.

Zhai D., Liu J., Zhang H., Yao M., Wang J. and Yang Y. (2014*b*) S-Pb isotopic geochemistry, U-Pb and Re-Os geochronology of the Huangganglang Fe-Sn deposit, Inner Mongolia, NE China. *Ore Geology Reviews*, **59**, 109–122.

Zhai D., Liu J., Zhang A. and Sun Y. (2017) U-Pb, Re-Os and $^{40}Ar/^{39}Ar$ geochronology of porphyry Sn ± Cu ± Mo and polymetallic (Ag–Pb–Zn-Cu) vein mineralization at Bianjiadayuan, Inner Mongolia, NE China: Implications for discrete mineralization events. *Economic Geology*, **112**, 2041–2059.

Zhai D., Liu J., Tombros S. and Williams-Jones A.E. (2018*a*) The genesis of the Hashitu porphyry molybdenum deposit, Inner Mongolia, NE China: constraints from mineralogical, fluid inclusion, and multiple isotope (H, O, S, Mo, Pb) studies. *Mineralium Deposita*, **53**, 377–397.

Zhai D., Liu J., Zhang H., Tombros S. and Zhang A. (2018*b*) A magmatic-hydrothermal origin for Ag–Pb–Zn vein formation at the Bianjiadayuan deposit, Inner Mongolia, NE China: Evidences from fluid inclusion, stable (C-H-O) and noble gas isotope studies. *Ore Geology Reviews*, **101**, 1–16.

Zhai D., Liu J., Cook N.J., Wang X., Yang Y., Zhang A. and Jiao Y. (2019) Mineralogical, textural, sulfur and lead isotope constraints on the origin of Ag–Pb–Zn mineralization at Bianjiadayuan, Inner Mongolia, NE China. *Mineralium Deposita*, **54**, 47–66.

Zhou J.B., Wilde S.A., Zhao G.C. and Han J. (2017) Nature and assembly of microcontinental blocks within the Paleo-Asian Ocean. *Earth-Science Reviews*, **186**, 76–93.